ADVANCED FUNCTIONAL MATERIALS
www.afm-journal.de

Check for updates

1D *p–n* Junction Electronic and Optoelectronic Devices from Transition Metal Dichalcogenide Lateral Heterostructures Grown by One-Pot Chemical Vapor Deposition Synthesis

Emad Najafidehaghani, Ziyang Gan, Antony George, Tibor Lehnert, Gia Quyet Ngo, Christof Neumann, Tobias Bucher, Isabelle Staude, David Kaiser, Tobias Vogl, Uwe Hübner, Ute Kaiser, Falk Eilenberger, and Andrey Turchanin**

Lateral heterostructures of dissimilar monolayer transition metal dichalcogenides provide great opportunities to build 1D in-plane *p–n* junctions for sub-nanometer thin low-power electronic, optoelectronic, optical, and sensing devices. Electronic and optoelectronic applications of such *p–n* junction devices fabricated using a scalable one-pot chemical vapor deposition process yielding $MoSe_2$-WSe_2 lateral heterostructures are reported here. The growth of the monolayer lateral heterostructures is achieved by in situ controlling the partial pressures of the oxide precursors by a two-step heating protocol. The grown lateral heterostructures are characterized structurally and optically using optical microscopy, Raman spectroscopy/microscopy, and photoluminescence spectroscopy/microscopy. High-resolution transmission electron microscopy further confirms the high-quality 1D boundary between $MoSe_2$ and WSe_2 in the lateral heterostructure. *p–n* junction devices are fabricated from these lateral heterostructures and their applicability as rectifiers, solar cells, self-powered photovoltaic photodetectors, ambipolar transistors, and electroluminescent light emitters are demonstrated.

1. Introduction

Monolayer transition metal dichalcogenides (TMD) such as MoS_2, WSe_2, $MoSe_2$, WSe_2, $NbSe_2$, etc. have been intensively studied in recent years owing to their unique electronic and optical properties for potential applications in ultrathin device technology.[1,2] TMD monolayers are available as *n*-type semiconducting ($MoSe_2$, MoS_2, WS_2),[3] *p*-type semiconducting (WSe_2),[4] metallic ($NbSe_2$, NbS_2),[5] and as semimetallic (WTe_2)[2,5] materials. The ability to connect them laterally in a single atomic plane provides opportunities to define a spatial modulation in electronic properties which is an absolute prerequisite for realizing sub-nanometer atomically thin TMD based device architectures including *p–n* junction diodes,[6–9] photodetectors,[6,10] photovoltaic devices,[7,11–13] space instruments,[14] electroluminescent,[6,13,15] and quantum devices.[6,16] Furthermore, lateral heterostructures provide unique opportunities to study physical phenomena in the 1D limit and may lead towards other unique applications.

Commonly used layer stacking techniques[17] of van der Waals layers are not applicable for the fabrication of 2D lateral heterostructures. Typically, a one-step[8,18–20] or a two-step[21–23] growth procedure either by physical vapor deposition (PVD)[18,19] or by

E. Najafidehaghani, Z. Gan, Dr. A. George, Dr. C. Neumann, Dr. D. Kaiser, Prof. A. Turchanin
Institute of Physical Chemistry
Friedrich Schiller University Jena
Lessingstr. 10, 07743 Jena, Germany
E-mail: antony.george@uni-jena.de; andrey.turchanin@uni-jena.de

Dr. T. Lehnert, Prof. U. Kaiser
Central Facility of Materials Science Electron Microscopy
Ulm University
Oberberghof 3/1, D-89081 Ulm, Germany

The ORCID identification number(s) for the author(s) of this article can be found under https://doi.org/10.1002/adfm.202101086.

© 2021 The Authors. Advanced Functional Materials published by Wiley-VCH GmbH. This is an open access article under the terms of the Creative Commons Attribution-NonCommercial-NoDerivs License, which permits use and distribution in any medium, provided the original work is properly cited, the use is non-commercial and no modifications or adaptations are made.

DOI: 10.1002/adfm.202101086

G. Q. Ngo, T. Bucher, Prof. I. Staude, Dr. T. Vogl, Dr. F. Eilenberger
Institute of Applied Physics
Friedrich Schiller University
Albert-Einstein-Str. 15, 07745 Jena, Germany

Prof. I. Staude
Institute of Solid State Physics
Friedrich Schiller University
Max-Wien-Platz 1, 07743 Jena, Germany

Dr. U. Hübner
Leibniz Institute of Photonic Technology (IPHT)
Albert-Einstein-Str. 9, 07745 Jena, Germany

Dr. A. George, T. Bucher, Prof. I. Staude, Dr. F. Eilenberger, Prof. A. Turchanin
Abbe Center of Photonics
Albert-Einstein-Straße 6, 07745 Jena, Germany

Dr. T. Vogl
Cavendish Laboratory
University of Cambridge
JJ Thomson Avenue, Cambridge CB3 0HE, UK

Dr. F. Eilenberger
Fraunhofer-Institute for Applied Optics and Precision Engineering IOF
Albert-Einstein-Str. 7, 07745 Jena, Germany

chemical vapor deposition (CVD)[22–24] is employed for growing TMD lateral heterostructures by lateral edge epitaxy.[18,20] A two-step growth procedure in which regions of different TMDs are grown one after another in subsequent growth experiments is the most common approach for obtaining TMD lateral heterostructures.[21–23] However, this method is difficult to scale up and the TMD layer grown initially has to be exposed to ambient conditions for the preparation of the second growth, which may have detrimental effects to the interface. In general, CVD is the most viable approach to produce TMDs due to its simplicity as well as lower growth temperatures in comparison with PVD techniques.[22–24] By employing a one-step CVD approach with suitable growth conditions, TMD lateral heterostructures can be grown sequentially by lateral edge epitaxy without exposure to ambient conditions.[24] However, such a growth procedure is challenging due to the possibility of precursor mixing, resulting in alloying, and subsequent poor quality of the *p–n* junction.

In this communication, we demonstrate a simple one-pot CVD method of large area $MoSe_2$-WSe_2 lateral heterostructures by subsequent selective evaporation of the metal oxide precursors by adjusting their precursor partial pressures during the growth process using differential heating. We have characterized the grown lateral heterostructures by optical microscopy (OM), Raman spectroscopy, atomic force microscopy (AFM), and photoluminescence (PL) spectroscopy for probing their morphological, structural, and optical properties. Furthermore, we have employed aberration-corrected high-resolution transmission electron microscopy (HRTEM) and high-angle annular dark-field scanning transmission electron microscopy (HAADF-STEM) combined with energy-dispersive X-ray spectroscopy (EDX) to reveal the high-quality interface between the $MoSe_2$ and WSe_2 areas of the lateral heterostructure. We have then realized atomically thin electronic and optoelectronic *p–n* junction devices, which can be used as rectifiers and exhibit photovoltaic characteristics under illumination with light. Furthermore, we have demonstrated that the heterojunction devices can be employed as a self-powered photovoltaic photodetector or ambipolar field-effect transistor. Under suitable biasing conditions, we have observed electroluminescent emission from our devices showing their potential applicability as ultrathin light-emitting diodes (LEDs).

2. Results and Discussion

We used a modified CVD method which employs a Knudsen type effusion cell (Figure S1, Supporting Information) to deliver the chalcogen precursors for the growth of the lateral heterostructures.[25] This technique has been shown to produce high-quality transition metal disulfide monolayers.[26] A scheme of the CVD setup is presented in **Figure 1**a. The Se precursor was loaded into the quartz effusion cell (see page 5 Supporting Information) and placed upstream in an inner tube at the low-temperature zone of the furnace. The temperature of the Se precursor was maintained at ≈400 °C during the growth procedure. The MoO_3 and WO_3 precursors were placed on two different silicon substrates inside the inner quartz tube and located in the high-temperature zone of the furnace. We have mixed a certain amount of NaCl to the oxide precursors to promote faster evaporation of the oxides by forming highly volatile molybdenum oxychloride or tungsten oxychloride species.[27] The growth substrate was placed next to and downstream of the oxide precursors. We used Ar as a carrier gas to transport the precursors to the growth substrate. Our growth procedure has two different heating steps for growing the $MoSe_2$ and WSe_2 areas of the lateral heterostructure. The growth substrate together with the metal oxide precursors was initially heated to a temperature of 730 °C. At this temperature, a flow of H_2 was introduced. This temperature is sufficient for the evaporation of molybdenum oxychloride species which reacts with the incoming Se atoms forming the $MoSe_2$ monolayer areas on the growth substrate. The substrates were kept at this temperature for 30 min to ensure complete evaporation and removal of the Mo-containing precursor from the furnace. Next, the flow of H_2 was stopped and the temperature was increased to 800 °C. At this temperature, a flow of H_2 was reintroduced into the furnace. The samples were kept under this condition for the next 15 min for the growth of WSe_2. The WSe_2 nucleates and grows preferably at the edges of the $MoSe_2$ crystals by lateral edge epitaxy[18,22] forming the $MoSe_2$-WSe_2 lateral heterostructure. In addition, we tested the growth of WSe_2 at 730 °C (with similar conditions for the $MoSe_2$ growth) and no deposition of isolated WSe_2 crystals takes place. This experimental observation is supported by the thermodynamic assessment of the system (see page 6 and Figure S2, Supporting Information). At 730 °C, partial pressure of the Mo-containing species is ≈200 times higher than the partial pressure of the W-containing species, which indicates that MoO_3 precursor can evaporate completely already at 730 °C, (see Figures S2 and S3, Supporting Information). Moreover, a flow of H_2 is essential for the growth of both $MoSe_2$ and WSe_2 areas, as it facilitates fast reduction of the oxide precursors to maintain sufficient concentration of transition metal precursors during the growth.[28,29] Thus, by controlling vapor pressure of the precursors by temperature and H_2 flow rates, we could successfully grow large area $MoSe_2$-WSe_2 lateral heterostructures.

As can be seen from Figure 1b,c and **Figure 2**, the grown $MoSe_2$-WSe_2 heterostructures have mostly hexagonal, star-like, or triangular shape with typical lateral sizes of inner and outer areas of 20–60 μm (see also Figure S4, Supporting Information, for additional images and description). To study their topography, we characterized the lateral heterostructures with an AFM using the tapping mode. Thus, Figure 1d,e present the respective height and phase images of the area highlighted in Figure 1c with a dashed square. The height profile across the lateral heterostructure on the SiO_2 substrate, corresponding to the dashed line in Figure 1d, is shown as an inset. The estimated heterostructure height of 0.8 ± 0.3 nm corresponds well to the monolayer thickness. A boundary between $MoSe_2$ and WSe_2 areas can be recognized in the phase image (Figure 1e); however, as expected for an atomically flat sheet, the height variation is not observed between the areas covered with different TMDs. A root mean square roughness of the heterostructure areas (measured on an area of 5 × 5 μm^2) was found to be 0.3 ± 0.1 nm, which further confirms its atomic flatness.

Next, to confirm the structural identity of the $MoSe_2$ and WSe_2 areas, we performed Raman spectroscopy and microscopy measurements. In Figure 2a,b, we show Raman spectra recorded on the inner $MoSe_2$ area and the outer WSe_2 area of the lateral heterostructure presented in Figure 2a as an inset. The formation of $MoSe_2$ is confirmed by the A_{1g} peak at 240.5 cm^{-1} originating from the out-of-plane vibrations of the Se atoms and E_{2g} peak at

© 2021 The Authors. Advanced Functional Materials published by Wiley-VCH GmbH

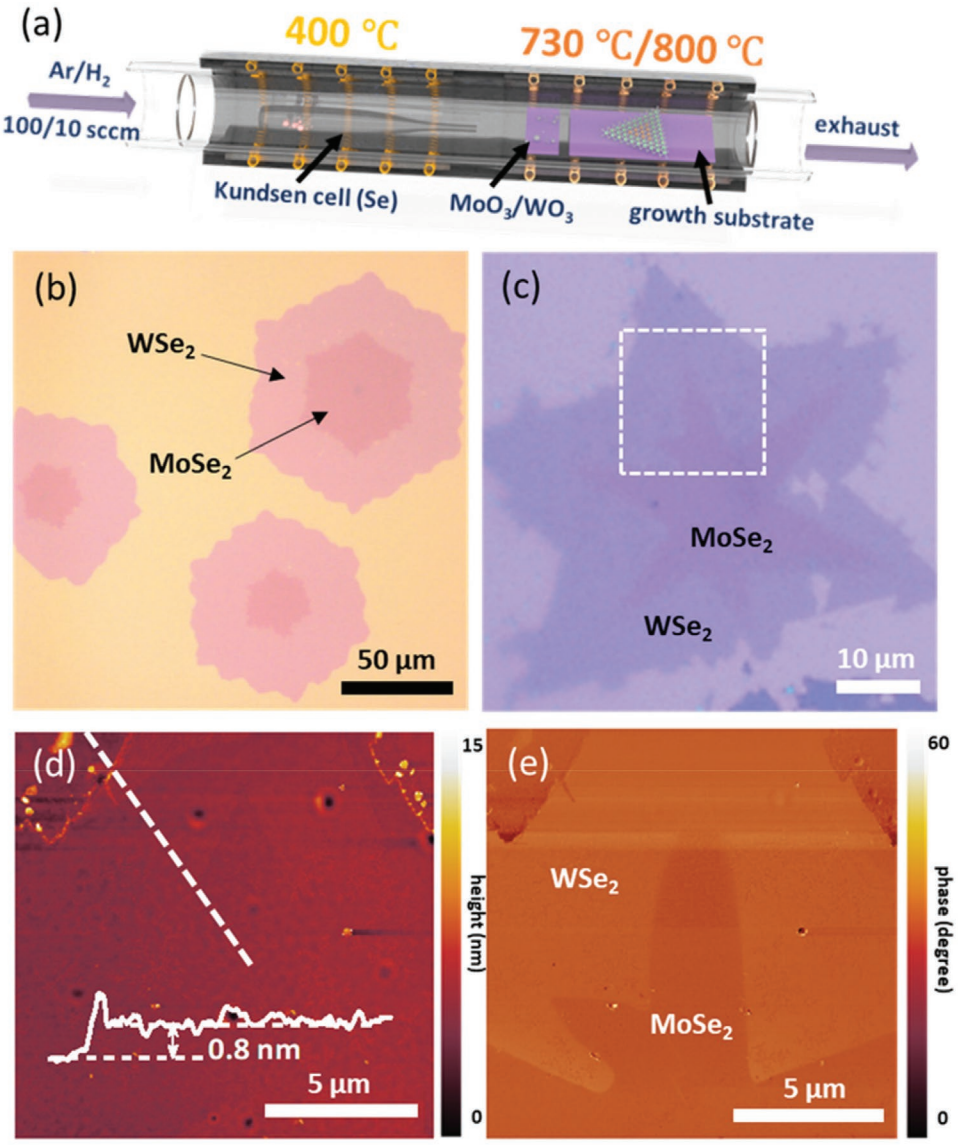

Figure 1. One-pot CVD growth of $MoSe_2$-WSe_2 lateral heterostructures. a) Schematic diagram of the CVD growth setup. b–c) OM images of $MoSe_2$-WSe_2 lateral heterostructures. False colors are used to enhance contrast between the $MoSe_2$ and WSe_2 areas. The area highlighted within the dashed square in (c) is imaged using an atomic force microscope in the tapping mode. d) AFM height image shows no contrast between the $MoSe_2$ and WSe_2 areas. The height profile between the SiO_2 substrate and the heterostructure is shown using solid white line (the height profile is extracted from the dashed white line). The thickness of the lateral heterostructure is estimated as 0.8 ± 0.3 nm which corresponding to a monolayer. Furthermore, there is no height difference between the $MoSe_2$ and WSe_2 areas, whereas they can be clearly recognized in the respective AFM phase image (e).

286 cm^{-1} originating from the in-plane vibrations of the Mo and Se atoms.[30] The A_{1g} peak at 250 cm^{-1} originating from the out-of-plane vibrations of the Se atoms confirms the formation of WSe_2, Figure 2b.[31,32] The 2LA(M) mode at 260.5 cm^{-1} originating from the longitudinal acoustic phonons, which are in-plane collective periodic compressions and expansions of atoms in the lattice, is also present in the WSe_2 spectra.[32] A Raman spectrum recorded at the border region of the $MoSe_2$ and WSe_2 areas is presented in Figure S5, Supporting Information, showing a superposition of the characteristic peaks of both materials. Intensity maps of the A_{1g} Raman modes of $MoSe_2$ and WSe_2 mapped on the entire $MoSe_2$-WSe_2 heterostructure are presented in Figure 2c,d, respectively. As seen from Figure 2c, intensity of the A_{1g} peak of $MoSe_2$ is only detected in the inner area of the heterostructure. Since the laser beam diameter was ≈1–2 µm, the $MoSe_2$ area appears to be slightly larger than the actual size. A line scan of Raman spectra recorded on a bigger lateral heterostructure is provided in Figure S6, Supporting Information. From the intensity map of the A_{1g} peak of WSe_2 presented in Figure 2d, it is evident that WSe_2 is only present in the outer area confirming the formation of the expected lateral heterostructure. Additionally, the chemical identity of the formed lateral heterostructure was confirmed by X-ray photoelectron spectroscopy (XPS) (see Figure S7, Supporting Information, for details).

The optical quality of the grown lateral heterostructures was probed by room-temperature PL measurements using a 532 nm

© 2021 The Authors. Advanced Functional Materials published by Wiley-VCH GmbH

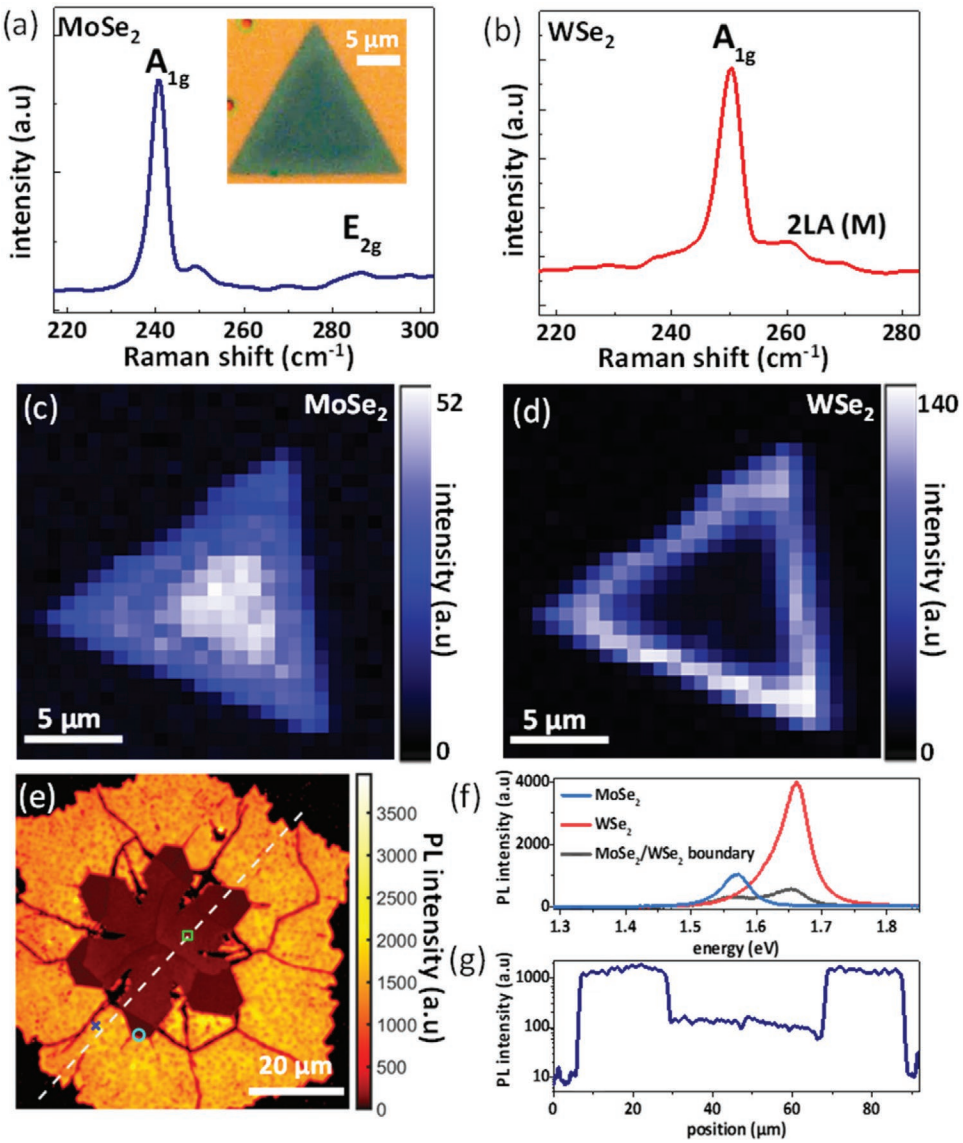

Figure 2. Raman spectroscopy and imaging of the $MoSe_2$-WSe_2 lateral heterostructures. A laser with $\lambda = 532$ nm is used to excite the Raman modes. a) Raman spectrum recorded on the $MoSe_2$ inner area showing the A_{1g} characteristic peak at 240.5 cm^{-1}. The inset shows an OM image of the $MoSe_2$-WSe_2 lateral heterostructure on which the Raman measurements are conducted. b) Raman spectrum recorded on the WSe_2 outer area of the heterostructure showing the A_{1g} peak at 250 cm^{-1}. c–d) Raman intensity map of the $MoSe_2$-WSe_2 heterostructure. In (c) the A_{1g} peak of $MoSe_2$ is mapped and in (d) the A_{1g} peak of WSe_2 is mapped. e–g) PL of the WSe_2-$MoSe_2$ lateral heterostructure. e) PL-map of the heterostructure, with indicators for the lineout in (f) and the positions at which PL-spectra have been measured in (g). f) PL-intensity along the lineout displayed in (e). The outer WSe_2-section has an intensity of 1700 ± 170 a.u., whereas the intensity of the inner $MoSe_2$-area has a brightness of 126 ± 20 a.u. g) Typical PL-spectra at the positions marked in (e) WSe_2 with a mean energy of 1.655 ± 0.03 eV and an FWHM of 0.16 ± 0.01 eV (red). $MoSe_2$ with a mean energy of 1.56 ± 0.02 eV and an FWHM of 0.06 ± 0.005 eV (blue). On the border with clear contributions by both materials (dark).

laser for the excitation. Figure 2e shows a PL spatial map of a $MoSe_2$-WSe_2 heterostructure. It can be seen that the inner part ($MoSe_2$) and the outer part (WSe_2) of the heterostructure show different PL intensities. As can be seen from the PL line profile (extracted from the dashed line in Figure 2e), the PL intensity from the WSe_2 is on average about 10 times higher than from the $MoSe_2$ (see Figure 2f); it is homogeneous for each material within ≈15%. Moreover, within the lateral resolution of the employed optical microscope (≈1 µm) a sharp border between two materials is observed, which excludes the formation of alloys on the respective length scale. Figure 2g presents the characteristic PL spectra acquired at the WSe_2 and the $MoSe_2$ areas as well as at the boundary region. For the $MoSe_2$ we measure an average peak wavelength of 790 nm (1.568 eV) with an FWHM bandwidth of 60 meV. For the WSe_2 an average peak wavelength of 748 nm (1.656 eV) with an FWHM bandwidth of 68 meV was detected. These values are consistent with the data reported for high-quality pristine monolayer crystals fabricated by CVD.[29,33] We, therefore, conclude that the fabricated heterostructure consists of well-separated areas, where these areas are

© 2021 The Authors. Advanced Functional Materials published by Wiley-VCH GmbH

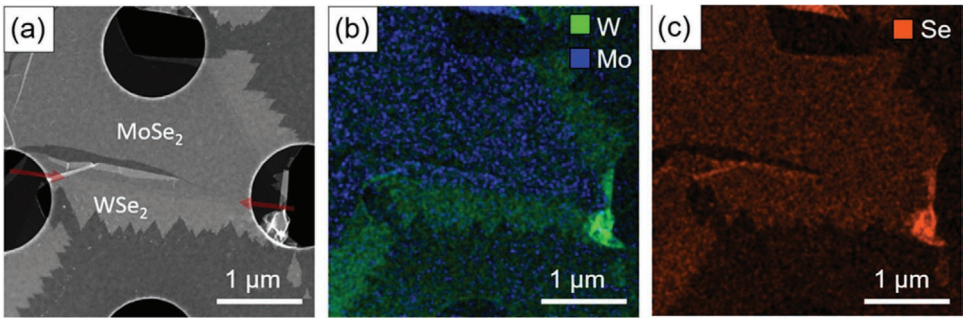

Figure 3. HAADF-STEM characterization of the $MoSe_2$-WSe_2 heterostructure. a) shows a 120 kV HAADF-STEM overview image of the lateral heterostructure on a holey-carbon TEM grid (the holes in the TEM grid appear black in the image and the greyish contrast originates from the flake of the lateral WSe_2 and $MoSe_2$ heterostructure, please notice its atomic-number-related contrast difference: deeper grey: $MoSe_2$, lighter grey: WSe_2). The corresponding EDX maps in (b) and (c) allow the identification of the element distribution: b) W (green), Mo (blue), and c) Se (orange).

of the same properties as the individual materials when they are grown separately. The PL observed for WSe_2 is stronger than that for $MoSe_2$. This difference is typical for our growth process and is likewise observed for individual material samples; hence we argue that the quality of neither material is degraded in the lateral heterostructure growth process.

To further characterize the lateral $MoSe_2$-WSe_2 heterostructure interface, we performed HAADF-STEM combined with EDX as well as chromatic (Cc) and spherical (Cs) aberration-corrected HRTEM. In **Figure 3**a, we show an overview HAADF-STEM image of the lateral heterostructure on a holey carbon TEM grid and Figure 3b,c demonstrate the corresponding Mo/W- and Se-EDX maps, respectively. The HRTEM unambiguously confirms the formation of a monolayer heterostructure (see Figure S8, Supporting Information), whereas the formation of large-sized $MoSe_2$ and WSe_2 areas, as well as a very straight boundary, are clearly revealed from HAADF-STEM (see red arrows in Figure 3a). Note that the edge of the WSe_2 area possesses a saw-toothed shape. As more electrons are scattered to higher angles from the heavier W in comparison to lighter Mo, the WSe_2 area appears brighter than that of $MoSe_2$. From the contrast analysis in Figure 3a and the respective EDX maps in Figure 3b,c we conclude that Se is homogeneously distributed on the whole heterostructure area, whereas Mo and W are present in the inner and outer regions, respectively. The EDX spectra were acquired over such long exposure time, the signal-to-noise ratio of the monolayer is small explaining very faint signals outside the flake originating from noise only.

Monolayer lateral heterostructures of *n-type* $MoSe_2$ and *p-type* WSe_2 enable the realization of atomically thin electronic and optoelectronic *p–n* junction devices. Next, we fabricated devices with the lateral heterostructures in two different configurations as shown schematically in **Figure 4**a,f. In the first type of device, the *p-type* WSe_2 and *n-type* $MoSe_2$ areas are connected in series with source and drain electrodes defined on each material as shown in Figure 4a. A current–voltage (*I–V*) characteristic of such a *p–n* junction diode device is shown in Figure 4b (Inset of 4b shows OM image). The rectification behavior of the diode can be observed from the *I–V* characteristics (i.e., the diode allowed electrical conduction only when it is operated in forward bias). Next, we tested the photoresponse of the device by irradiating it using a 520 nm laser. In Figure 4c, the *I–V* characteristics of a *p–n* junction device under dark and under illumination with varying intensities of the laser are shown. The device exhibits a dark current of 135 pA at a source-drain bias (V_{ds}) of 1 V. When irradiating the device, a clear photovoltaic effect can be observed. For instance, when irradiating with an intensity of 61 ± 5 mW cm^{-2} the device shows an open-circuit voltage (V_{OC}) of 0.24 V and a short-circuit current (I_{SC}) of 354 pA. The fill factor (FF) of the device is calculated as 0.27. The power conversion efficiency (PCE), that is, the ratio of output electrical power to the incident light power can be calculated using the equation, $\mathrm{PCE} = \frac{I_{sc} \times V_{oc} \times \mathrm{FF}}{P_{incident}}$, where $P_{incident}$ is the incident laser power. The PCE is calculated as 0.12%, which is similar to the reported values on similar TMD-based junctions.[11,23,34] We have fabricated and characterized five *p–n* junction heterostructure devices and all of the devices show similar behavior. We estimated the photoresponse also theoretically (see Figure S9, Supporting Information) using density functional theory (DFT) calculations by adding the electron–photon interaction into the device Hamiltonian employing the first-order perturbation theory,[35] see page 8 Supporting Information. The onset of the photocurrent was found at a photon energy of 2.35 eV, just below the 520 nm of the laser light applied experimentally. However, the calculations also show that the photocurrent is sensitive to the doping level of the devices and to the defect concentration. For a doped junction, the onset of the photocurrent was found at a lower photon energy of 2.15 eV and the photocurrent is larger compared to the undoped junction. Hence, this result can be considered as a qualitative proof of the applicability of the heterostructures devices in a photovoltaic cell.

In Figure 4d and Figure 4e we show the optical response of the device with alternating light pulses ($\lambda = 520$ nm, 61 ± 5 mW/cm^2). The data in Figure 4d is acquired without any applied V_{ds} demonstrating a self-powered photovoltaic photodetector. The rise (τ_{rise}) and fall (τ_{fall}) time constants of photocurrent can be estimated by fitting the curves using a single exponential growth and decay function as shown in Figure S11a, Supporting Information. The τ_{rise} and τ_{fall} are estimated as 0.16 ± 0.01 s and 0.15 ± 0.01 s respectively when the photodetector is operated without any applied bias. The on/off ratio of the photodetector is in the order of 10^4 at V_{ds} = 0 V without the application of a gate voltage. The data in Figure 4e is acquired with an applied bias, V_{ds} = +0.5 V and applied gate voltage, V_g = −20 V. We applied a V_g = − 20 V to adjust the off current to a minimum. In this case, the on/off ratio of the device is estimated in the order of 10^2 and the τ_{rise} and τ_{fall} are estimated as 0.17 ± 0.01 s

© 2021 The Authors. Advanced Functional Materials published by Wiley-VCH GmbH

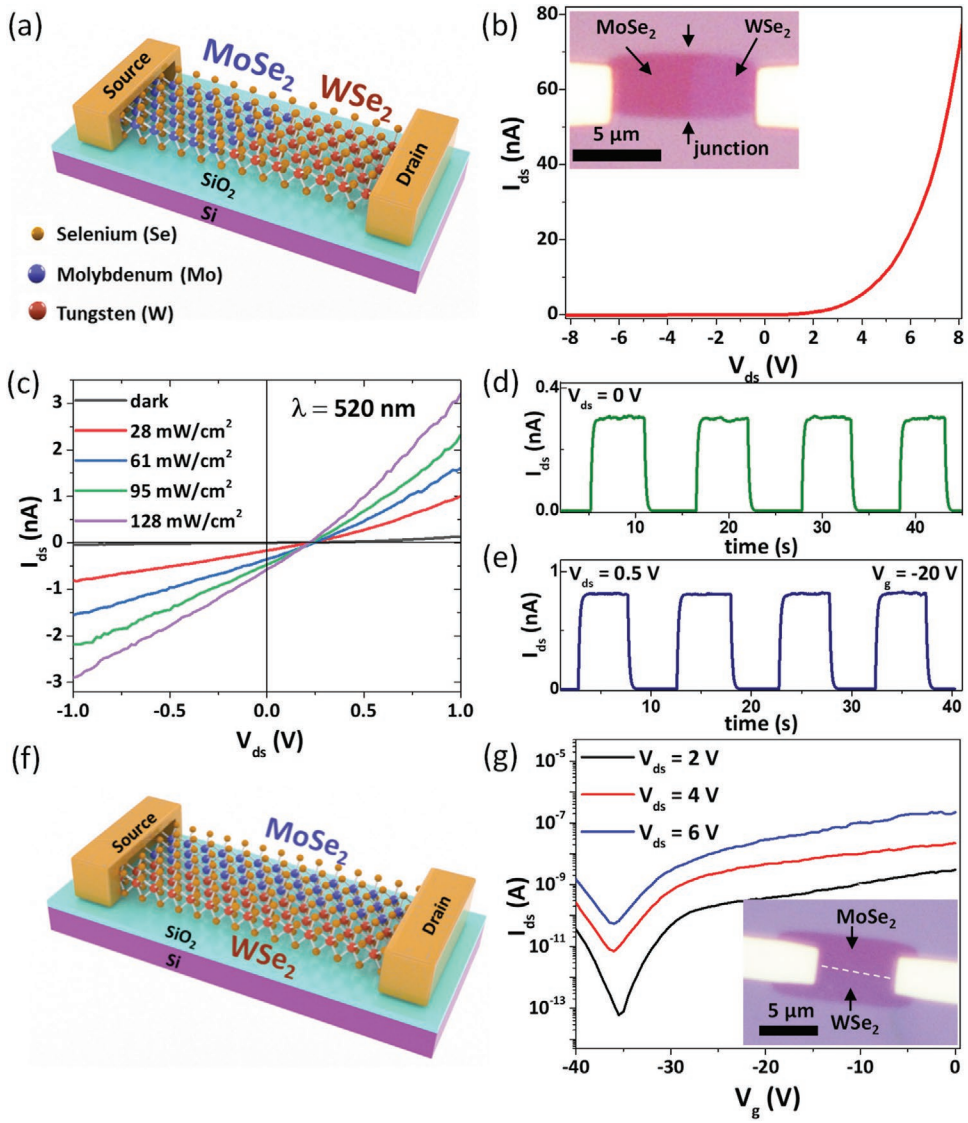

Figure 4. Electronic and optoelectronic characterization of *p–n* junction devices fabricated using the $MoSe_2$-WSe_2 lateral heterojunctions. a) Scheme of the *p–n* junction device. b) The *I–V* curve of $MoSe_2$-WSe_2 lateral heterostructure *p–n* junction device shows strong rectification behavior. The inset shows an OM image of the device. The *p–n* junction device channels are lithographically defined to enable the charge transport only in the precise device channel contrary to previously published reports.[15,18,21] c) The *I–V* characteristics of the *p–n* junction device at dark and under illumination ($\lambda = 520$ nm) with varying laser intensities. The photovoltaic response of the *p–n* junction device can be clearly observed. d–e) Light pulses are applied to the device using a laser with $\lambda = 520$ nm at an intensity of 61 mW cm^{-2} and the optical response is measured as a function of time. d) The device shows photovoltaic response to the light without applying a source-drain bias (photovoltaic photodetector). Even a higher photoresponse is observed when the device is measured by applying a $V_{ds} = +0.5$ V and a $V_g = -20$ V (e). The analysis of the rise and fall time constants of photocurrent is shown in Figure S9, Supporting Information. f–g) Characterization of ambipolar field-effect transistors fabricated using $MoSe_2$-WSe_2 parallel channels. f) Schematic of the ambipolar field-effect transistor device. g) Transfer characteristics recorded at different source-drain voltages (V_{ds}) show ambipolar transport behavior. An OM image of the device is shown in the inset. The dashed white line represents the boundary between $MoSe_2$ and WSe_2.

and 0.15 ± 0.01 s respectively (Figure S11b, Supporting Information). We estimated the responsivity of the photodetector, that is, the photocurrent generated per unit power of the incident light using the equation $R_\lambda = \frac{I_{ph} - I_{dk}}{P_{incident}}$, where R_λ is the responsivity, I_{ph} is the photocurrent, and I_{dk} is the dark current. In the photovoltaic photodetector operation mode, the responsivity is estimated as 18 mA W^{-1} at an incident laser power of 28 ± 5 mW cm^{-2}. With an applied $V_{ds} = +1$ V, the responsivity is estimated as 110 mA W^{-1}. In Figure S12, Supporting Information, we show the tunability of responsivity with respect to V_{ds} (at $V_g = 0$ V) when irradiating with an intensity of 28 ± 5 mW cm^{-2} extracted from the data presented in Figure 4c. The external quantum efficiency (EQE) of the device, that is, the ratio of number of photo-induced carriers to the number of incident photons of the device can be estimated using the equation, $\eta = R_\lambda \times \frac{hc}{\lambda e} \times 100\%$, where h is the Planck's constant, c is the speed of light, λ is the wavelength of light used, and e is

© 2021 The Authors. Advanced Functional Materials published by Wiley-VCH GmbH

the electron charge. In the photovoltaic photodetector operation mode ($V_{ds} = 0$), the EQE is calculated as 4.3%. When applying $V_{ds} = +1$ V the EQE is 23.4%. The detectivity (d^*) of a photodetector can be calculated using the equation $d^* = R_\lambda \sqrt{\frac{S}{2eI_{dk}}}$; where S is the effective area of the photodetector. The detectivities are calculated as 1×10^9 Jones and 6×10^8 Jones at $V_{ds} = 0$ and $V_{ds} = +1$ V, respectively. The figures of merit of the heterostructure photodetector are comparable to previously reported photodetectors fabricated using TMD-based materials and junctions.[36] When operating at the photovoltaic mode, the photodetector shows a high on/off ratio in the order of 10^4, which is higher than most of the previously reported TMD-based photodetectors. Such self-powered optoelectronic devices are desirable building blocks for energy-efficient electronic equipment since no additional energy supply is required. Additionally, we performed electrical and optoelectronic measurements on devices made of individually grown $MoSe_2$ and WSe_2 monolayers (see pages 9-10 Supporting Information for details and Figures S13–S16, Supporting Information for the OM, AFM, Raman, and XPS characterization of individually grown monolayers of $MoSe_2$ and WSe_2). These devices do not show any rectification/photovoltaic effect, which demonstrates that the presence of the p–n junctions due to the 1D $MoSe_2$-WSe_2 boundary is responsible for the rectification, photovoltaic, and self-power photodetector effects (see pages 9-10 and Figures S17–S19, Supporting Information).

The second type of devices was fabricated in such a way that the $MoSe_2$ and WSe_2 areas were connected in parallel to the source-drain electrodes as shown schematically in Figure 4f. The junction between the p and n region is in the middle perpendicular to the electrodes. Such devices with parallel p-type (WSe_2) and n-type ($MoSe_2$) channels are expected to function as ambipolar field-effect transistors.[37] The ambipolar transistors are promising building blocks for applications including lighting, display, memory, logic, and neuromorphic computing devices.[35] An OM image of an ambipolar transistor is shown in the inset of Figure 4g. We performed field-effect transport measurements on such devices and transfer characteristics, that is, the enhancement of drain current with applied V_g at different applied V_{ds}, are shown in Figure 4g. The transfer characteristics demonstrate ambipolar transport as expected. In such a device configuration, the p-channel (WSe_2) becomes conductive towards negative V_g and the $MoSe_2$ n-channel becomes conductive towards more positive V_g. It can be seen that the minimum conductivity points of the transfer curves shifted towards the negative gate voltages possibly due to substantial n-doping induced by the SiO_2 substrate as well as the transfer process.[38]

The serial p–n junction devices were also tested for their suitability as electroluminescent photon emitters. The devices were operated under forward bias voltage with both current and light emission measured in the process. The light emission was measured using a high-resolution camera through a microscopic objective. The camera images displayed in **Figure 5**a,b clearly show that light is detected in a diffraction-limited spot on the position of the heterostructure junction only if voltage is supplied. A series of images with varying supply voltages were recorded together with the device current. The results are displayed in Figure 5c. Light emission onset can be observed at a voltage of roughly 50 to 60 V, with typical electrical currents in the microampere range. Light emission could be observed reproducibly over hours for voltages up to 100 V. Considering the number of detected photons and the detection efficiency of the setup, we estimate the internal quantum efficiency of the emission process to be in the range of 10^{-7}. High operation voltages are assumed to originate from the contacts operating in the Schottky mode as well as due to high channel resistance.

3. Conclusion

In summary, we have demonstrated a simple and reproducible method to synthesize large-area monolayer lateral heterostructures of $MoSe_2$ and WSe_2 by controlling the precursor evaporation in a scalable one-pot CVD process. The grown heterostructures were characterized using optical and AFM, Raman, and XPS as well as PL measurements to reveal their morphological, structural, chemical, and optical quality. Using TEM, we have confirmed the high quality of 1D boundary between the $MoSe_2$ and WSe_2 in their lateral heterostructure. We fabricated p–n junction devices using the synthesized heterostructures and demonstrated their applicability as rectifiers, photovoltaic cells (solar cells), self-powered photodetectors,

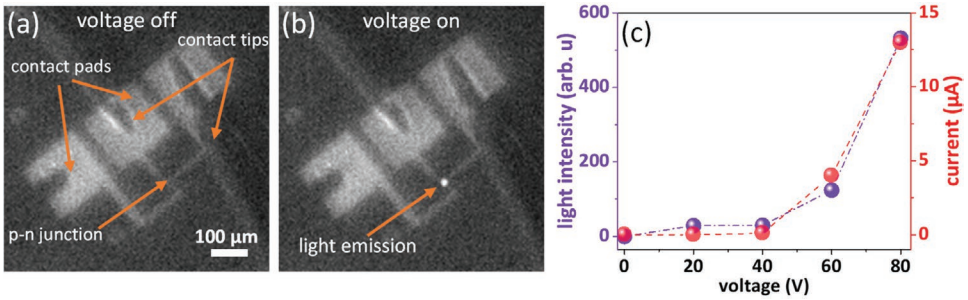

Figure 5. LED type emission from the monolayer $MoSe_2$-WSe_2 lateral heterostructure p–n junction device. a) Microscope image of the heterostructure in voltage "off" state and with and applied voltage of 60 V ("on") via the square contact pads. Light emission is seen as a bright spot of diffraction-limited size appearing at the heterostructure location. b) Light intensity and current through the junction as a function of input voltage (the dashed lines are provided as a guide to the eye).

© 2021 The Authors. Advanced Functional Materials published by Wiley-VCH GmbH

and light-emitting devices. Furthermore, we demonstrated the possibility of ambipolar field-effect transistors using laterally connected parallel $MoSe_2$-WSe_2 channels. We expect that high-quality 1D *p–n* junctions are of high interest for solid-state physics in general, as they pose an opportunity to study the impact of the dimensionality on the dynamics of excitations in solid-state boundaries. We also anticipate that our findings will facilitate the ongoing search for sub-nanometer, non-silicon electronic, optoelectronic, and photovoltaic devices.

Supporting Information

Supporting Information is available from the Wiley Online Library or from the author.

Acknowledgements

The authors acknowledge financial support of the Thüringer MWWDG via the "ProExzellenz 2014–2019" programme under the grants "ACP^{Explore}2016" and "ACP^{Explore}2018" as well as the Deutsche Forschungsgemeinschaft (DFG) through a research infrastructure grant INST 275/257-1 FUGG and CRC 1375 NOA (Project B2 and Project B3). This project has also received funding from the joint European Union's Horizon 2020 and DFG research and innovation programme FLAG-ERA under grant TU149/9-1. T.L. and U.K. acknowledge funding from the DFG and the Ministry of Science, Research and the Arts (MWK) of the federal state of Baden-Württemberg (Germany) in the frame of the SALVE project (www.salve-project.de), as well as the European Union in the frame of the Graphene Flagship. F.E. and T.V., acknowledge support by the Federal Ministry of Education and Science of Germany under Grant ID 13XP5053A. F.E. was supported by the Max Planck School of Photonics. E.N. and Q.G.N. are supported by the European Union, the European Social Funds and the Federal State of Thuringia under Grant ID 2018FGR00088. The authors thank Stephanie Höppener and Ulrich S. Schubert for enabling the Raman spectroscopy and microscopy studies at the Jena Center for Soft Matter (JCSM).

Open access funding enabled and organized by Projekt DEAL.

Conflict of Interest

The authors declare no conflict of interest.

Author Contributions

E.N. and Z.G. contributed equally to this work. A.G. and A.T. conceived the research and designed the experiments. Z.G., E.N., and A.G. synthesized the lateral heterostructures by CVD and performed basic material characterizations. Z.G. performed the thermodynamic analysis to interpret the growth process. C.N. performed Raman spectroscopy and XPS. T.B. and F.E. performed the PL spectroscopy and analysis with the guidance of I.S. T.L. and U.K. performed the HRTEM and HAADF-STEM analysis. U.H. fabricated the electrical devices. E.N., A.G., and D.K.performed the electrical/optoelectronic measurements and data analysis. G.Q.N., F.E., and E.N. performed the electroluminescence measurements. T.V. performed the DFT calculations and interpretation. A.G., F.E., and A.T. wrote the manuscript with input from all authors.

Data Availability Statement

The data that support the findings of this study are available from the corresponding author upon reasonable request.

Keywords

lateral heterostructures, light-emitting diode, *p–n* junction, transition metal dichalcogenides monolayers, 2D devices

Received: February 22, 2021
Revised: March 23, 2021
Published online:

[1] a) S. Manzeli, D. Ovchinnikov, D. Pasquier, O. V. Yazyev, A. Kis, *Nat. Rev. Mater.* **2017**, *2*, 17033; b) Z. Cai, B. Liu, X. Zou, H.-M. Cheng, *Chem. Rev.* **2018**, *118*, 6091.
[2] W. Choi, N. Choudhary, G. H. Han, J. Park, D. Akinwande, Y. H. Lee, *Mater. Today* **2017**, *20*, 116.
[3] N. Choudhary, M. A. Islam, J. H. Kim, T.-J. Ko, A. Schropp, L. Hurtado, D. Weitzman, L. Zhai, Y. Jung, *Nano Today* **2018**, *19*, 16.
[4] H. Zhou, C. Wang, J. C. Shaw, R. Cheng, Y. Chen, X. Huang, Y. Liu, N. O. Weiss, Z. Lin, Y. Huang, X. Duan, *Nano Lett.* **2015**, *15*, 709.
[5] A. Kuc, T. Heine, A. Kis, *MRS Bull.* **2015**, *40*, 577.
[6] R. Frisenda, A. J. Molina-Mendoza, T. Mueller, A. Castellanos-Gomez, H. S. J. van der Zant, *Chem. Soc. Rev.* **2018**, *47*, 3339.
[7] S. Lei, X. Wang, B. Li, J. Kang, Y. He, A. George, L. Ge, Y. Gong, P. Dong, Z. Jin, G. Brunetto, W. Chen, Z.-T. Lin, R. Baines, D. S. Galvão, J. Lou, E. Barrera, K. Banerjee, R. Vajtai, P. Ajayan, *Nat. Nanotechnol.* **2016**, *11*, 465.
[8] Y. Gong, J. Lin, X. Wang, G. Shi, S. Lei, Z. Lin, X. Zou, G. Ye, R. Vajtai, B. I. Yakobson, H. Terrones, M. Terrones, B. K. Tay, J. Lou, S. T. Pantelides, Z. Liu, W. Zhou, P. M. Ajayan, *Nat. Mater.* **2014**, *13*, 1135.
[9] a) L. Liu, N. Xu, Y. Zhang, P. Zhao, H. Chen, S. Deng, *Adv. Funct. Mater.* **2019**, *29*, 1807893; b) C.-Y. Lin, X. Zhu, S.-H. Tsai, S.-P. Tsai, S. Lei, Y. Shi, L.-J. Li, S.-J. Huang, W.-F. Wu, W.-K. Yeh, Y.-K. Su, K. L. Wang, Y.-W. Lan, *ACS Nano* **2017**, *11*, 11015.
[10] W. Wu, Q. Zhang, X. Zhou, L. Li, J. Su, F. Wang, T. Zhai, *Nano Energy* **2018**, *51*, 45.
[11] C.-H. Lee, G.-H. Lee, A. M. van der Zande, W. Chen, Y. Li, M. Han, X. Cui, G. Arefe, C. Nuckolls, T. F. Heinz, J. Guo, J. Hone, P. Kim, *Nat. Nanotechnol.* **2014**, *9*, 676.
[12] M.-L. Tsai, M.-Y. Li, J. R. D. Retamal, K.-T. Lam, Y.-C. Lin, K. Suenaga, L.-J. Chen, G. Liang, L.-J. Li, J.-H. He, *Adv. Mater.* **2017**, *29*, 1701168.
[13] A. Pospischil, M. M. Furchi, T. Mueller, *Nat. Nanotechnol.* **2014**, *9*, 257.
[14] T. Vogl, K. Sripathy, A. Sharma, P. Reddy, J. Sullivan, J. R. Machacek, L. Zhang, F. Karouta, B. C. Buchler, M. W. Doherty, Y. Lu, P. K. Lam, *Nat. Commun.* **2019**, *10*, 1202.
[15] M.-Y. Li, J. Pu, J.-K. Huang, Y. Miyauchi, K. Matsuda, T. Takenobu, L.-J. Li, *Adv. Funct. Mater.* **2018**, *28*, 1706860.
[16] C. Palacios-Berraquero, M. Barbone, D. M. Kara, X. Chen, I. Goykhman, D. Yoon, A. K. Ott, J. Beitner, K. Watanabe, T. Taniguchi, A. C. Ferrari, M. Atatüre, *Nat. Commun.* **2016**, *7*, 12978.
[17] a) R. Frisenda, E. Navarro-Moratalla, P. Gant, D. Pérez De Lara, P. Jarillo-Herrero, R. V. Gorbachev, A. Castellanos-Gomez, *Chem. Soc. Rev.* **2018**, *47*, 53; b) H. Xue, Y. Wang, Y. Dai, W. Kim, H. Jussila, M. Qi, J. Susoma, Z. Ren, Q. Dai, J. Zhao, K. Halonen, H. Lipsanen, X. Wang, X. Gan, Z. Sun, *Adv. Funct. Mater.* **2018**, *28*, 1804388; c) W. Gao, F. Zhang, Z. Zheng, J. Li, *ACS Appl. Mater. Interfaces* **2019**, *11*, 19277.
[18] P. K. Sahoo, S. Memaran, Y. Xin, L. Balicas, H. R. Gutiérrez, *Nature* **2018**, *553*, 63.
[19] C. Huang, S. Wu, A. M. Sanchez, J. J. P. Peters, R. Beanland, J. S. Ross, P. Rivera, W. Yao, D. H. Cobden, X. Xu, *Nat. Mater.* **2014**, *13*, 1096.

© 2021 The Authors. Advanced Functional Materials published by Wiley-VCH GmbH

[20] F. Ullah, Y. Sim, C. T. Le, M.-J. Seong, J. I. Jang, S. H. Rhim, B. C. Tran Khac, K.-H. Chung, K. Park, Y. Lee, K. Kim, H. Y. Jeong, Y. S. Kim, *ACS Nano* **2017**, *11*, 8822.
[21] K. Chen, X. Wan, J. Wen, W. Xie, Z. Kang, X. Zeng, H. Chen, J.-B. Xu, *ACS Nano* **2015**, *9*, 9868.
[22] Y. Zhang, L. Yin, J. Chu, T. A. Shifa, J. Xia, F. Wang, Y. Wen, X. Zhan, Z. Wang, J. He, *Adv. Mater.* **2018**, *30*, 1803665.
[23] M.-Y. Li, Y. Shi, C.-C. Cheng, L.-S. Lu, Y.-C. Lin, H.-L. Tang, M.-L. Tsai, C.-W. Chu, K.-H. Wei, J.-H. He, W.-H. Chang, K. Suenaga, L.-J. Li, *Science* **2015**, *349*, 524.
[24] J. Lee, S. Pak, Y.-W. Lee, Y. Park, A. R. Jang, J. Hong, Y. Cho, B. Hou, S. Lee, H. Y. Jeong, H. S. Shin, S. M. Morris, S. Cha, J. I. Sohn, J. M. Kim, *ACS Nano* **2019**, *13*, 13047.
[25] A. George, C. Neumann, D. Kaiser, R. Mupparapu, T. Lehnert, U. Hübner, Z. Tang, A. Winter, U. Kaiser, I. Staude, A. Turchanin, *J. Phys.: Mater.* **2019**, *2*, 016001.
[26] S. Shree, A. George, T. Lehnert, C. Neumann, M. Benelajla, C. Robert, X. Marie, K. Watanabe, T. Taniguchi, U. Kaiser, B. Urbaszek, A. Turchanin, *2D Mater.* **2019**, *7*, 015011.
[27] S. Li, S. Wang, D.-M. Tang, W. Zhao, H. Xu, L. Chu, Y. Bando, D. Golberg, G. Eda, *Appl. Mater. Today* **2015**, *1*, 60.
[28] a) B. Liu, M. Fathi, L. Chen, A. Abbas, Y. Ma, C. Zhou, *ACS Nano* **2015**, *9*, 6119; b) H. Wang, D. Zhu, F. Jiang, P. Zhao, H. Wang, Z. Zhang, X. Chen, C. Jin, *Nanotechnology* **2018**, *29*, 314001.
[29] J.-K. Huang, J. Pu, C.-L. Hsu, M.-H. Chiu, Z.-Y. Juang, Y.-H. Chang, W.-H. Chang, Y. Iwasa, T. Takenobu, L.-J. Li, *ACS Nano* **2014**, *8*, 923.
[30] J. Xia, X. Huang, L.-Z. Liu, M. Wang, L. Wang, B. Huang, D.-D. Zhu, J.-J. Li, C.-Z. Gu, X.-M. Meng, *Nanoscale* **2014**, *6*, 8949.
[31] a) P. Tonndorf, R. Schmidt, P. Bottger, X. Zhang, J. Borner, A. Liebig, M. Albrecht, C. Kloc, O. Gordan, D. R. Zahn, S. Michaelis de Vasconcellos, R. Bratschitsch, *Opt. Express* **2013**, *21*, 4908; b) X. Zhang, X.-F. Qiao, W. Shi, J.-B. Wu, D.-S. Jiang, P.-H. Tan, *Chem. Soc. Rev.* **2015**, *44*, 2757.
[32] M. Yang, X. Cheng, Y. Li, Y. Ren, M. Liu, Z. Qi, *Appl. Phys. Lett.* **2017**, *110*, 093108.
[33] X. Wang, Y. Gong, G. Shi, W. L. Chow, K. Keyshar, G. Ye, R. Vajtai, J. Lou, Z. Liu, E. Ringe, B. K. Tay, P. M. Ajayan, *ACS Nano* **2014**, *8*, 5125.
[34] a) F. Wang, Z. Wang, K. Xu, F. Wang, Q. Wang, Y. Huang, L. Yin, J. He, *Nano Lett.* **2015**, *15*, 7558; b) S. Jia, Z. Jin, J. Zhang, J. Yuan, W. Chen, W. Feng, P. Hu, P. M. Ajayan, J. Lou, *Small* **2020**, *16*, 2002263; c) M. M. Furchi, A. Pospischil, F. Libisch, J. Burgdörfer, T. Mueller, *Nano Lett.* **2014**, *14*, 4785; d) Y. Deng, Z. Luo, N. J. Conrad, H. Liu, Y. Gong, S. Najmaei, P. M. Ajayan, J. Lou, X. Xu, P. D. Ye, *ACS Nano* **2014**, *8*, 8292; e) N. Flöry, A. Jain, P. Bharadwaj, M. Parzefall, T. Taniguchi, K. Watanabe, L. Novotny, *Appl. Phys. Lett.* **2015**, *107*, 123106.
[35] M. Palsgaard, T. Markussen, T. Gunst, M. Brandbyge, K. Stokbro, *Phys. Rev. Appl.* **2018**, *10*, 014026.
[36] a) J. Yao, G. Yang, *Nanoscale* **2020**, *12*, 454; b) M. Long, P. Wang, H. Fang, W. Hu, *Adv. Funct. Mater.* **2019**, *29*, 1803807.
[37] Y. Ren, X. Yang, L. Zhou, J.-Y. Mao, S.-T. Han, Y. Zhou, *Adv. Funct. Mater.* **2019**, *29*, 1902105.
[38] M. Amani, M. L. Chin, A. L. Mazzoni, R. A. Burke, S. Najmaei, P. M. Ajayan, J. Lou, M. Dubey, *Appl. Phys. Lett.* **2014**, *104*, 203506.

© 2021 The Authors. Advanced Functional Materials published by Wiley-VCH GmbH